ELSEVIER

Infrared Physics & Technology 40 (1999) 247–259

INFRARED PHYSICS & TECHNOLOGY

www.elsevier.com/locate/infrared

Development of a high-power THz radiation source for plasma diagnostics

M.R. Siegrist [a,*], H. Bindslev [b], R. Brazis [c], D. Guyomarc'h [a], J.P. Hogge [a], Ph. Moreau [a], R. Raguotis [c]

[a] *Centre de Recherches en Physique des Plasmas, Ecole Polytechnique Fédérale de Lausanne, CRPP-PPB, 1015 Lausanne, Switzerland*
[b] *FOM-Instituut voor Plasmafysica 'Rijnhuizen', Postbus 1207, 3430 BE Nieuwegein, Netherlands*
[c] *Semiconductor Physics Institute, A. Goštauto 11, 2600 Vilnius, Lithuania*

Abstract

A high power radiation source in the THz range with long pulse and narrow line width is required for diagnosing fusion type plasmas by collective Thomson scattering. Gyrotrons currently meet the requirements concerning power, pulse length and line width when operating in the 50–150 GHz range. They may have the potential also to do this in the THz range. In this paper two methods based on harmonic operation are investigated. Both look promising, if high conversion efficiency can be attained. This, however, still has to be demonstrated.

PACS: 42.65.Ky; 84.40.Ik; 52.70.m

Keywords: Plasma diagnostics; Harmonic generation; High frequency source; Gyrotron; Diffraction grating; Semiconductors

1. Collective Thomson scattering as diagnostic tool of fusion type plasmas

For fusion type plasmas, and in particular for ITER, collective Thomson scattering (CTS) is being considered as a diagnostic of

- confined fast ion distributions (fusion alpha particles),
- the fuel ratio in the plasma center and
- poloidal plasma rotation.

In CTS it is the collective fluctuations of the electrons that are being probed. These fluctuations are principally driven by the ion dynamics, which is why CTS, though scattering off the electrons, provides information about the ions. The collective fluctuations dominate the uncorrelated electron fluctuations, which carry no ion information, at scale lengths larger than the Debye length, λ_D. Thus, for the collective fluctuations to dominate we generally require that the wave vector k^S of the resolved fluctuations satisfies the inequality

$$k^S \lambda_D < 1 \tag{1}$$

where $k^S = k^s - k^i$. Here k^i and k^s are the wave vectors of the incident and received scattered radiation, respectively. To satisfy Eq. (1) for a given plasma and thus λ_D, requires either a large wavelength for the incident radiation or a small scattering angle. The latter approach has limits, since the scat-

* Corresponding author. E-mail: mark.siegrist@epfl.ch.

1350-4495/99/$ - see front matter
PII: S1350-4495(99)00015-8

tered radiation must be separated from the input beam.

Another requirement for a successful CTS experiment is to avoid spectral regions of strong absorption in the plasma and intense plasma background radiation. The former makes the inner part of the plasma inaccessible and the latter reduces the signal-to-noise ratio. Both can render a measurement impossible. Plasma electron cyclotron absorption (ECA) and emission (ECE) are the main causes of absorption and emission in the wavelength range considered. The situation is illustrated for an ITER type plasma in Figs. 1 and 2. The first shows the optical depth as a function of frequency for X-mode. Clearly in X-mode the center of the plasma is only accessible at frequencies below 100 GHz or above 1 THz. In O-mode the plasma is also accessible in a narrow frequency band around 190 GHz, which falls between the fundamental and the second harmonic of the electron cyclotron resonance. Fig. 2 shows the radiation temperature for X-mode radiation as a function of frequency. Although we noted the plasma

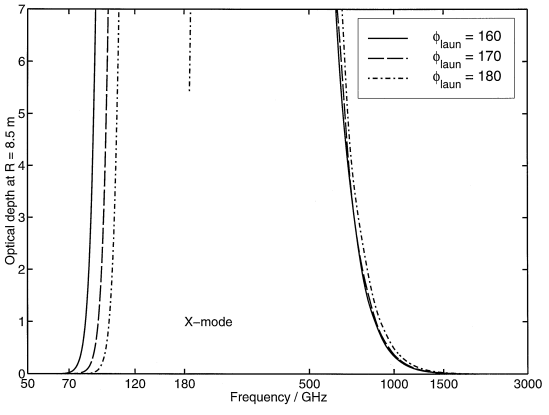

Fig. 1. Optical depth from the low field side of the plasma to a major radius of 8.5 m for an ITER like equilibrium, as a function of radiation frequency for X-mode and a range of viewing angles Φ_{laun}. Φ_{laun} is the azimuthal angle of the viewing direction with $\Phi_{\text{laun}} = 180°$ corresponding to viewing in the $x-z$ plane. Viewing position is at $x = 11.0$ m, $y = 0.0$ m, $z = 1.25$ m and $\Phi_{\text{laun}} = 84°$. The temperature profile is peaked with a maximum of 27.6 keV while the density profile is flat with a maximum of 1.27×10^{20} m^{-3} and the central magnetic field is 5.7 T. The frequency scale is logarithmic. The curves show that in X-mode access to the central part of the plasma from this viewing position is only possible at frequencies below 100 GHz for a limited range of azimuthal viewing directions, and above 1 THz.

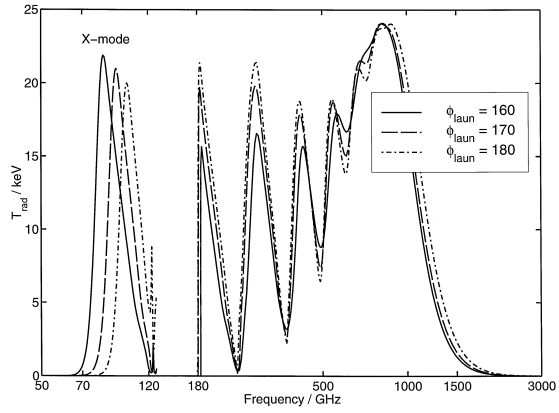

Fig. 2. Radiation temperature T_{rad} as a function of frequency for the same plasma, viewing position and viewing directions considered in Fig. 1. The sharp structure at frequencies just above 120 GHz is due to the cold electron cyclotron resonance and R-cutoff entering at the low field side plasma edge. The feature in the frequency range 70 to 120 GHz is ECE at the relativistically Doppler down-shifted fundamental cyclotron resonance. This computation of the radiation temperature assumes that the walls act as cold black bodies. T_{rad} thus represents a lower estimate of the radiation temperature for the given plasma in the situations where the plasma is not optically thick and wall reflections would contribute to T_{rad}.

is accessible above 1 THz, the radiation is quite intense up till 1.5 THz. In O-mode the radiation temperature falls off more rapidly at high frequencies, but because the plasma is only weakly absorbing around 1 THz in both modes, wall reflections, not screened by the plasma, will cause some X-mode radiation to be converted to O-mode. These curves are very sensitive to the electron temperature profile, assumed here to be peaked with a maximum of 28 keV.

The following probing frequencies and sources have been considered for fast ion diagnosis:

1. A 60–80 GHz gyrotron, injected as X-mode below the fundamental electron cyclotron resonance ν_{ce} and above the L-cutoff.
2. A 170–250 GHz gyrotron, injected as O-mode between ν_{ce} and 2 times ν_{ce}.
3. A 1 to 1.2 THz radiation source (3rd harmonic gyrotron), operating in the high frequency tail of the ECE spectrum.
4. A 1.5–3 THz (free electron laser), operating above the ECE spectrum.

5. A 28.28 THz CO_2 laser far above the ECE spectrum.

Comments on options [1] are as follows.

(1) Existing CTS experiments have given some experience with the technologies required for the gyrotron based options 1 and 2. Though a number of practical problems persist, the required technological developments are minor. Option 1 would make use of an operating window which is narrow in frequency and launch angle. This, combined with refraction, may be expected to give rise to operational difficulties and encumber interpretation. Extensive investigations of the diagnostic potential have been carried out.

(2) ECE is strong in this frequency range and must be expected to be present at the level of 10 keV or more for all viewing directions because of wall reflections. To detect the CTS signal it would be necessary to reduce the ECE background noise with a viewing dump; either in the form of a physical structure or by using the cold region of the fundamental cyclotron resonance. The former is incompatible with the first wall requirements and the latter would meet considerable operational difficulties. Extensive investigations of the diagnostic potential have been carried out.

(3) To investigate this option a new ECE emission code has been developed (fully relativistic and without expansion in a small Larmor radius parameter). Initial indications are that the higher frequencies will be required to reduce the ECE. High power, long pulse 3rd harmonic gyrotron emission at these frequencies has not yet been demonstrated. Research into the feasibility of such sources is ongoing. Detailed studies of the diagnostic potential and source requirements have not yet been carried out.

(4) Free electron lasers as sources for CTS suffer from short pulse lengths and broad line widths, which at present appear to rule out this option.

(5) This option would use a CO_2 laser as source. The optimal power is in the 10 MW range with a total pulse time of the order of 100 μs (can be delivered as a sequence of shorter pulses). The power figure assumes the currently reported noise/efficiency of the broad band quantum well detectors, which would provide the first mixer in a heterodyne detection system. These detectors are currently subject to intense research and development. Though CO_2 laser based scattering systems have been used extensively for fluctuation measurements, the technique has not yet been demonstrated for fast ion CTS. Such experience is likely to become available through the CO_2 laser-based CTS experiment currently being installed at JT60U. Extensive investigations of diagnostic potential have been carried out, but they rely on many untested assumptions about the performance of the equipment.

The fuel ratio and poloidal plasma rotation can be diagnosed with a separate CTS system of the type described in option 1.

This indicates that a range of options exist and all have their advantages and disadvantages. None of them has really been fully tested and number 3 (the one we want to concentrate on) has as much potential as any of them. Depending on the frequency which can finally be reached, it is either possible to operate in the tail or even completely outside the ECE emission region. The required pulse duration of the order of ms is no problem and neither is the power, assuming it can indeed be frequency-converted with high efficiency.

It should also be remembered that the decision to build ITER has still not been reached. Thereafter it will take years to build it or a similar machine and then again some years of basic machine operation and physics studies, before there will be alpha particles to be diagnosed. So talking about the development of the source in light of the fact that sources for most other options exist, is not ruled out by time scales.

2. High-frequency gyrotrons

The gyrotron is a high-power microwave source based on the maser instability: the resonant interaction of a weakly relativistic electron beam gyrating in an external magnetic field, and the eigenmode of an electromagnetic cavity. The unique features of gyrotrons are:

- high interaction efficiency (~ 35% overall efficiency, ~ 50% with energy recovery system)
- single mode operation
- availability of sources ranging from centimetric to submillimetric wavelengths

– high power (from a few watts up to 1 MW depending on pulse length) and high energy per pulse (up to 3.6 MJ at 170 GHz, 450 kW, [2]).

The gyrotron is considered as the best candidate for a wide spectrum of applications ranging from fusion plasma heating, profile control, current drive, and diagnostics for fusion plasmas, to industrial microwave sintering [3] or to electron paramagnetic resonance (EPR, [4]) studies.

The emission frequency ω of a gyrotron is related to the magnetic field strength B_0 in the interaction region through

$$\omega \approx \Omega_e = \frac{eB_0}{\gamma m_0} \tag{2}$$

where m_0 is the rest mass of the electrons and γ the relativistic factor. Hence, in principle, all that is required to achieve a high emission frequency is to provide a strong enough magnetic field. Unfortunately technical limits are approached rather soon when one talks about frequencies of several 100 GHz, in particular, if high power is desired as well. Magnets producing several tesla are available with small bore diameters, but this is incompatible with high power operation because of the thermal wall loading of the resonant gyrotron cavity inside the magnet bore. In the frequency range of 100–200 GHz, suitable for the heating of fusion plasmas by means of electron cyclotron resonance absorption, gyrotrons which supply powers of up to 1 MW are nowadays available [5] with pulse lengths approaching 1 s, or even several seconds at somewhat lower power [6]. On the other hand, a Japanese group has reported a gyrotron operating at 850 GHz with a power in the region of 100 W [7].

Existing high-power gyrotrons could be used in two different ways to produce high powers at high frequencies.

(1) The gyrotron itself can be operated at a higher harmonic of its fundamental frequency. In this way the magnets have to be able to provide only the field strength corresponding to the fundamental frequency. The efficiency will be somewhat reduced, but can reach values almost comparable with those at the fundamental frequency [8], in particular if simultaneous operation at the fundamental can be suppressed.

(2) The radiation of a gyrotron can be frequency upconverted externally by means of suitable nonlinear materials. A large range of such materials exist and have been investigated. The main problem is the usually small conversion efficiency which can possibly be overcome by carefully optimized experimental arrangements (multi-pass systems, for example).

3. Quasi-optical gyrotron with diffraction grating

In contrast to the so-called conventional gyrotron in which the electron beam and the resonant cavity are coaxial, the symmetry axis of the resonator in a quasi-optical gyrotron (QOG) is perpendicular to the magnetic axis. While this arrangement has a negative influence on the suppression of parasitic oscillations possibly generated in the electron beam drift structure [9] and on the interaction efficiency, it offers great flexibility as far as resonator design is concerned. In particular, it allows for Fabry–Perot type resonators consisting of two spherically curved mirrors to be used. In resonators of this type, the beam is usually coupled out either by diffraction around one of the mirrors or through slits in the mirror. Both methods result in a significant degradation of the microwave beam quality. At laser frequencies this problem has been overcome by the use of semi-transparent mirrors. Unfortunately they do not exist in the gyrotron wavelength range and certain approximations (wire meshes or grids, perforated metal mirrors) cannot usually sustain the high radiation power density. An almost ideal solution is the use of a diffraction grating. This takes the form of a curved metal mirror with sinusoidal grooves (see Fig. 3). The resonator axis is aligned to coincide with the -1 order of the grating, whereas the output coupling takes place along the order zero. This implies that the coarse shape (neglecting the grooves) of the mirror takes the form of an off-axis imaging mirror which re-focuses the output beam in order to pass it through the output window with flat phase fronts (see Fig. 4). The groove separation and depth have to be designed in order to match the mode structure in the equivalent Fabry–Perot type resonator and also to obtain the desired equivalent reflectivity and transmittivity of the grating [10].

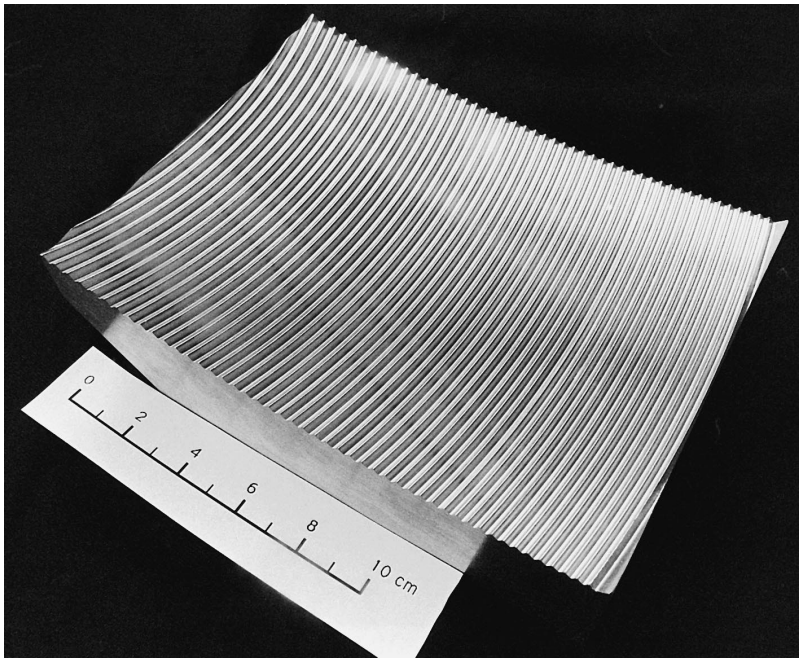

Fig. 3. Photo showing the curved diffraction grating with sinusoidal grooves.

For a beam incident on a grating with an angle θ, the Littrow condition for the diffraction order -1 can be written as

$$2\sin\theta = \frac{\lambda}{d} \tag{3}$$

where d is the grating period. If the additional constraint

$$\lambda/d > 2/3 \tag{4}$$

is imposed, then only the diffraction orders 0 and -1 can propagate, ensuring that no power is diffracted elsewhere. In the case where these two conditions are fulfilled for the third harmonic of the cyclotron frequency, the Littrow condition cannot be met for the fundamental or the second harmonic and oscillations at those frequencies cannot be destabilized in order to grow.

In Fig. 4 we show a cut through such a resonator set-up with grating. A resonator of this type has been designed and is ready for in situ cold-testing, using the configuration shown in Fig. 4. At this stage, low power sources and detection set-up were available around 100 GHz only and 2 different gratings were used.

– One existing grating designed for operation at 91 GHz [11], in order to characterize the resonances and the diffraction output pattern.

– A new grating designed for operation at 270 GHz, on which measurements were made at 90 GHz to check the absence of resonance at subharmonics. Measurements at frequencies around 270 GHz with this grating are planned in the near future.

Fig. 5 top shows a spectrum analyzer trace of the signal diffracted at the order 0 when the cavity with the first grating (designed for 91 GHz) is fed through a small hole drilled in the center of the spherical mirror (see Fig. 4). Vertical lines indicate the frequencies of several TEM_{oo} modes obtained from the resonator parameters, in very good agreement with the measured resonances. The measured quality factors for the corresponding modes are also shown on the bottom of Fig. 5. The computer-controlled XY-scanner allowed us to obtain intensity profiles in the plane of the output window. Such a measurement is

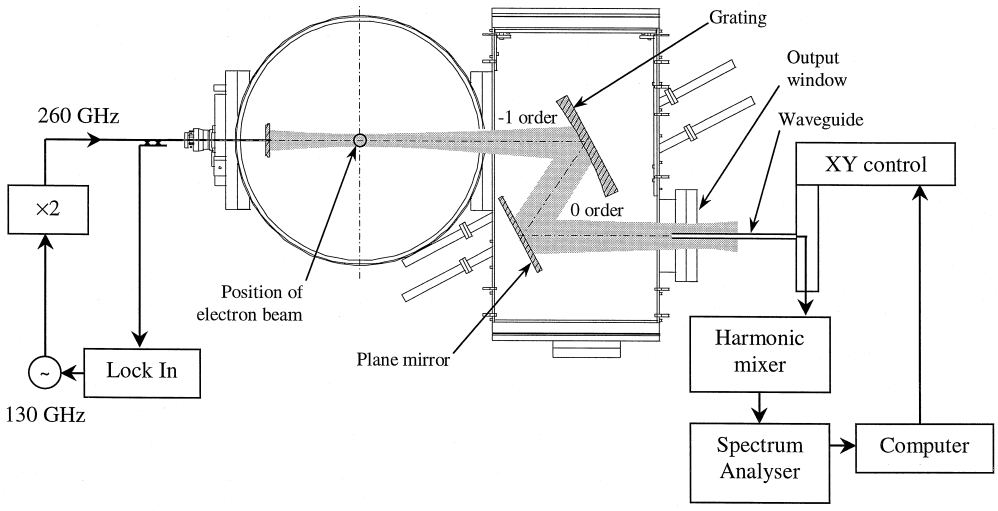

Fig. 4. Top view of the resonant cavity of the quasi-optical gyrotron. The elements used for cold-testing as well as the position of the electron beam (not present during cold-tests) are shown. In this arrangement, the magnetic field and the electron beam path are perpendicular to the page.

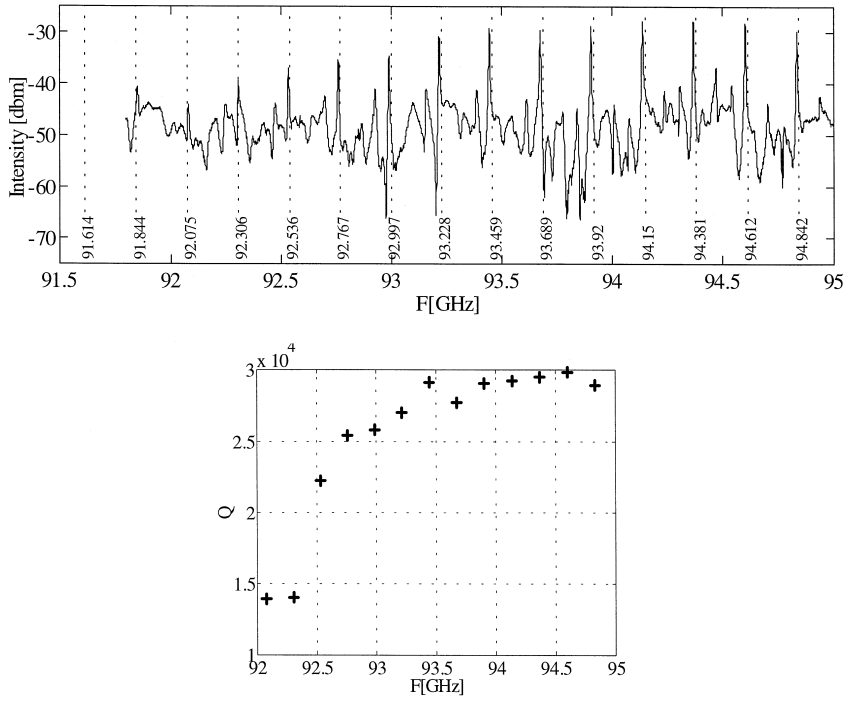

Fig. 5. Results of cold-test measurements of the resonator designed for operation at the fundamental frequency. Solid trace: spectrum analyzer output trace. Vertical dotted lines: calculated frequencies of corresponding modes. The measured quality factor Q is also shown.

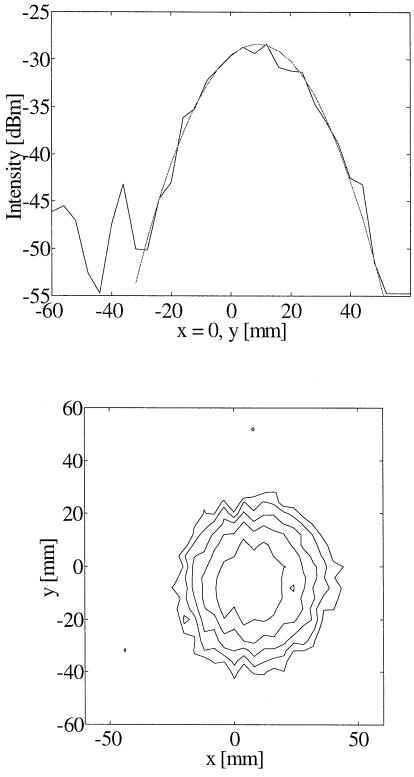

Fig. 6. The beam profile of a particular mode in one and two dimensions, including a Gaussian fit.

reproduced in Fig. 6 in one and two dimensions. It can be fitted very accurately with a Gaussian profile, in agreement with theoretical predictions.

The second grating (designed for 270 GHz) was then mounted on the same experimental set-up. As expected, no evidence of the existence of resonances at frequencies around 90 GHz could be found.

We will finally report about a design study for a quasi-optical gyrotron operating at the third harmonic at 280 GHz. It is based on an existing gyrotron at the CRPP and is planned to be used for a proof of principle demonstration.

Simulations of the electron beam trajectories have been performed with the DAPHNE code [12]. As input the following parameters have to be provided:

– electron gun geometry
– geometry and currents of the superconducting coils
– modulating and accelerating anode voltages
– electron beam current
– number of particles to be simulated.

An adaptive spatial mesh is used in DAPHNE and the field and electron beam parameters are calculated at each mesh point. The procedure is as follows:

– The external electric field is calculated from Laplace's equation. The boundary conditions are the potential on the electrodes.
– The external magnetic fields are calculated from the Bio-Savart law.
– The particle trajectories are obtained from Newton's equation of motion in an electrostatic field.
– The space charge electric field in the drift region caused by the electron beam is calculated from the Poisson equation at each mesh point.

Several iteration stages involving the last two points lead to convergence. The output of DAPHNE consists in the electron trajectories as well as beam statistics.

In our particular case an existing gun, designed to operate at 92 GHz, will be used. The parameters are given in Table 1. The beam–radiation interaction efficiency was obtained from a one-dimensional gyrotron equilibrium code [13]. Fig. 7 shows the results of efficiency calculations. The expected efficiency is about 8%. In order to achieve an output power level of 200 kW a beam current of 30 A is required. DAPHNE simulations of this electron gun indicated that space charge effects on the cathode may affect the beam for currents over 30 A. The simulations showed that the velocity spreads are reasonable: $\Delta\nu_{\|}/\langle\nu_{\|}\rangle = 6.3\%$ and $\Delta\nu_{\perp}/\langle\nu_{\perp}\rangle = 3.9\%$. The spread in the velocity pitch factor (defined as $\nu_{\perp}/\nu_{\|}$) was rather high: 9.3%. In order to reduce this spread, the anode shape was slightly modified. It was possible to decrease both the axial and the transverse velocity spreads and the spread in the pitch factor.

The spread in electron energy is the main reason for the gyrotron efficiency degradation [14]. Since

Table 1

Parameter	Value
Beam current I_b	30 A
Beam voltage U_b	80 kV
Cyclotron frequency f_{co}	91.5 GHz
Velocity ratio α	1.3
Average radius of guiding centers	3 mm

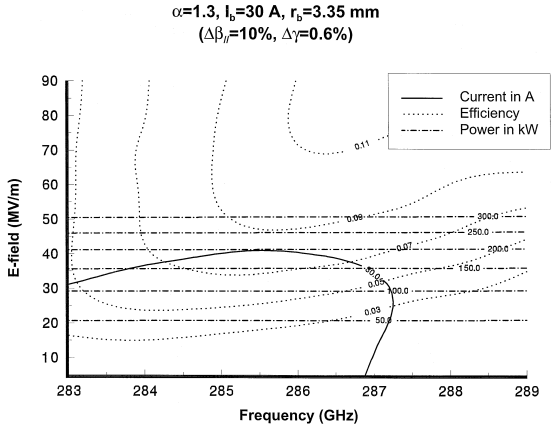

Fig. 7. Simulation results of the beam-radiation coupling efficiency and power of the gyrotron designed for third harmonic operation.

DAPHNE is an equilibrium code, it was only possible to simulate the energy spread based on DC space charge effects in the beam tunnel. It was found that this spread grows with increasing current, but remains low ($\approx 0.04\%$) for a current of 30 A. The negative mass instability [14,15] may give a dominant contribution to the electron energy spread. Numerical simulations and comparison with existing gyrotrons have shown that the dominant factor in the growth of the instability is the magnetic field gradient which should be kept as high as possible in order to minimize the spatial extent over which the cyclotron frequency matches the resonance condition. In addition, the beam tunnel should not be too long.

According to these simulations a gyrotron operating at the third harmonic frequency of 280 GHz based on a conventional quasi-optical gyrotron should be able to produce significant output power (≈ 200 kW). If this can be confirmed by the experiments in preparation, scaling to higher frequencies will be investigated.

4. Passive frequency conversion

The conversion by nonlinear materials of a sizable fraction of an electromagnetic wave to a wave at a harmonic frequency is by now well known. This technique has been applied with great success in particular in the visible part of the spectrum, where very impressive conversion efficiencies of more than half of the initial power have been achieved [16]. A range of experiments have also been reported in the mm and FIR regions [17–23]. Theoretical and experimental investigations have shown that different semiconductor materials exhibit significant gain at higher harmonics in the frequency range of interest. However, the highest efficiency achieved so far was only 0.1% in the normal incidence experiments on n-type silicon plates [21–23]. The limitations were given by a surface breakdown effect which precluded pumping of the material with higher powers, and by saturation effects observed below the breakdown threshold. Considerably higher nonlinear susceptibilities need to be revealed if the problem is to be solved by judicious choice of material alone.

We will first present a theoretical and numerical discussion of the problem, followed by preliminary experimental results.

5. Third harmonic generation in semiconductors

The primary idea [17] of efficient harmonic generation is based on the cubic relation between the forward-emitted 3rd harmonic intensity I_3 and the pumping wave intensity I_1 incident on a slab of thickness d

$$I_3 = \frac{32\pi}{c}|T_c\,\chi_3 C(d)|^2 I_1^3, \tag{5}$$

where c is the speed of light, χ_3 is the third-order nonlinear susceptibility understood as the coefficient in the expansion of the polarization in the power series of electric field E: $P = \chi_1 E + (\chi_3 E^2)E + \cdots$. T_c accounts for the electric field discontinuity at the front and back boundaries of the slab [24] and $C(d)$ is the thickness-dependent phase matching factor.

If the 3rd order susceptibility as well as T_c and $C(d)$ are independent of the wave amplitude, then Eq. (5) implies that a sufficiently high pump intensity is all that is required to obtain high intensity and efficiency of 3rd harmonic generation. In contrast to this, experiments on n-type Si crystals have shown that the 3rd harmonic intensity deviates from the cubic increase and finally saturates with rising pump wave intensity [21]. The cause of saturation is found in the change of electron scattering and their effec-

tive mass in the high-amplitude pumping wave electric field.

The problem is to find semiconductor materials and operating temperatures with high χ_3 and geometrical arrangements to increase T_c in order to get higher third harmonic generation (THG) efficiency. Let us consider electrons in the conduction band as the only source of non-linearity. Assuming constant electron density, we focus our attention on the electron drift non-linearity. Monte Carlo modeling provides the time dependence of the drift velocity $V(t)$ of electrons in the pumping wave field varying in time as $\boldsymbol{E}_1 \cos \omega_1 t$. Fourier-transformation applied to $V(t)$ then gives the drift velocity components $V_N \cos(\omega_N t + \psi_N)$ where ψ_N is the drift velocity phase and N the harmonic number. Following the relation $\partial \boldsymbol{P}/\partial t = ne\boldsymbol{V}$, where e is the elementary charge, one gets the equivalence [23]

$$\chi_3 = i \frac{ne}{3\omega_1 \varepsilon_0 E_1^2} \left(\frac{V_3}{E_1} \right) \tag{6}$$

where ε_0 is the free-space dielectric constant, and the ratio of V_3 and E_1 is complex due to the phase shift.

The phase matching function $C(d)$ in low-loss materials exhibits Maker's [25] oscillations when the sample thickness is increased. In highly absorbing materials the function shows a single maximum at a certain sample thickness mainly determined by the loss: therefore the maximum does not present any guide for the harmonic output optimization in this case. Instead of seeking for a thickness-controlled maximum, we focus here on thin samples so as to reduce the Joule loss, and to reveal electronic factors controlling the output power and efficiency. With the assumptions that the free-electron contribution to ε is small compared to the lattice one (ε_L), and the slab thickness d is small enough to satisfy the condition

$$d \ll \sqrt{\frac{\varepsilon_L}{\mu_0}} \frac{2}{ne} \left(\frac{E_1}{V_1} \right) \tag{7}$$

where μ_0 is the free-space magnetic constant, the 3rd harmonic intensity can be expressed as

$$I_3 = K \left(\frac{2}{1 + \sqrt{\varepsilon_L}} \right)^2 \left| \frac{endV_3}{E_1} \right|^2 I_1 \tag{8}$$

where K is a physical constant independent of the material and field parameters. The last expression states that the efficiency $\eta_3 = I_3/I_1$ is proportional to the square of the 3rd harmonic surface current density at a given pumping wave amplitude. If the surface carrier density nd is constant, the 3rd harmonic output power is governed by the 3rd harmonic drift velocity amplitude at the pumping wave field amplitude E_1.

We determined the 3rd harmonic drift velocity dependency on E_1 using Monte Carlo techniques. The algorithm of MC simulations in an alternating electric field follows the standard procedure [26]. It involves the intra- and intervalley scattering of electrons, and the band nonparabolicity.

6. Results

Simulations have been done at three different frequencies, viz. 9.43, 118 and 333 GHz. The choice of 333 GHz was made because its third harmonic is just the magic 1 THz frequency we attempt to reach with this procedure. The gyrotron which will be installed at CRPP this autumn will have a frequency of 118 GHz. It is planned to be used for third harmonic ECR heating of the TCV tokamak. However, during almost one year it will be available for experiments on third harmonic generation in solid-state materials. These experiments are currently under preparation. The simulations at 9.43 GHz, on the other hand, allow us a direct comparison of predictions with measurements using a magnetron as source. These experiments were conducted at the Institute of Semiconductor Physics in Vilnius, Lithuania.

Details of the results obtained in Si, GaAs and InP have been published elsewhere [27] and will not be repeated in detail. The main findings shown in Fig. 8 are the following.

- In all three materials an efficiency maximum is observed at power levels significantly below the breakdown threshold. Hence it will be possible to operate at this efficiency maximum point. The fact that such a point exists is not surprising. As pointed out above in connection with Eq. (5), the conversion efficiency grows with increasing pump power in the low power regime. At very high power the drift amplitude saturation due to randomization of the

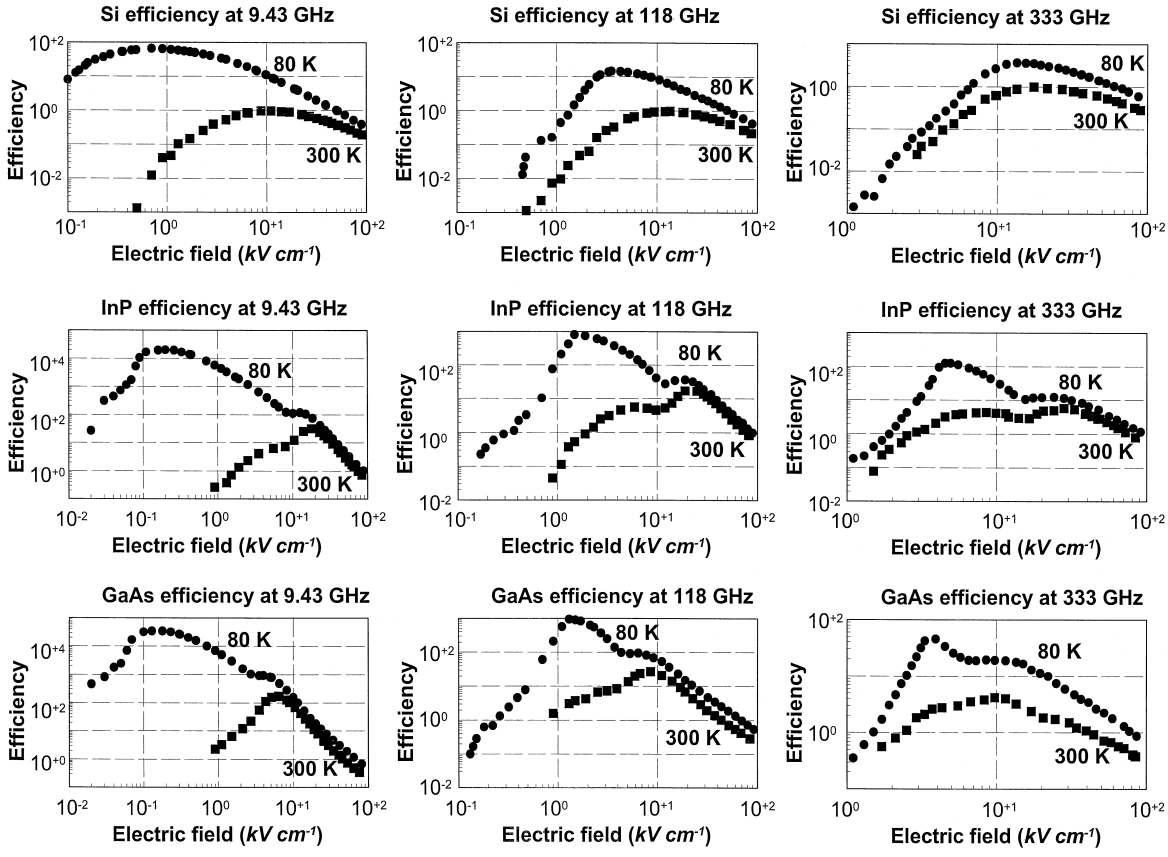

Fig. 8. Calculated conversion efficiency I_3/I_1 for three materials, three frequencies and two temperatures. All curves are normalized to the efficiency maximum for silicon at room temperature.

electron momentum by phonon emission and absorption reduce the efficiency again. Hence an efficiency maximum is expected in the medium power range.

· Cooling of the sample to liquid nitrogen temperature can increase the conversion efficiency by orders of magnitude. Indeed, at low temperature, the electron moves freely in the electric field until it acquires enough energy to emit a high energy phonon. This threshold phenomenon is leading to an increase of the third harmonic efficiency by orders of magnitude. An important requirement is to use pure crystals in order to prevent carrier scattering on ionized impurities and other defects. The thermal conductivity of all three materials studied becomes comparable or better than in copper and hence efficient cooling of the sample during long pulse or cw operation seems feasible, provided that the thin nonlinear layer is epitaxially grown on the thermally conductive but electrically insulating substrate.

· Experiments at 9.43 GHz have confirmed qualitatively the main results of simulations.

In the simulations performed so far only thin samples have been considered and hence no optimization of the absolute conversion efficiency has yet been attempted. The experimental results at 9.43 GHz gave efficiencies below the current record of 0.1% reported in Ref. [21]. Unfortunately the frequency dispersion in these materials is significant, as is the nonlinear absorption at the fundamental frequency. Hence increasing the sample thickness to attain phase-matched conditions over large distances is of very limited use, whereas multi-passing of the harmonic beam might result in significant improvements.

7. Resonant enhancement of the conversion efficiency

To conclude we will discuss the effect of a nonlinear sample inside a Fabry–Perot type resonator. Such a resonator occurs naturally, even without any additional reflecting surfaces around the sample, because of the refractive index discontinuities associated with the sample surfaces. We take as an example a silicon slab with a doping concentration of $n_e = 1.7 \times 10^{13}$ cm^{-3}, corresponding to an available sample. The coefficients T and R for the silicon air boundary can be determined from the complex refractive index n_ω at the fundamental frequency, which corresponds to a wavelength of 676 μm for the particular case considered here [21].

For the sample and wavelength considered this yields $|T| = 0.45$. While the fringe contrast at the fundamental frequency is not very pronounced for such a low quality resonator (see Fig. 9), the effect on the third harmonic is quite dramatic (Fig. 10) with a resonant amplitude enhancement of 40! This follows from the detailed analysis of all forward and backward propagating waves and their mutual coupling inside the sample, as discussed in detail in Ref. [24]. It must be emphasized, however, that it has been assumed in these calculations that the third harmonic current density is and remains proportional to the third power of the electric field amplitude at the fundamental. This assumption obviously breaks down at some stage, when the power at the fundamental or the third harmonic reaches appreciable values. A more detailed analysis would be required to simulate the situation with such saturation effects included.

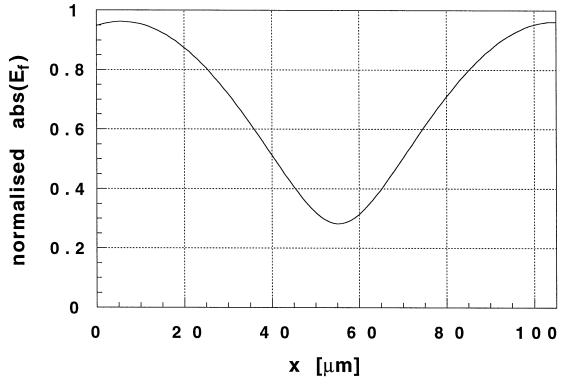

Fig. 9. Field enhancement due to the Fabry–Perot effect inside a Si slab at the pump frequency.

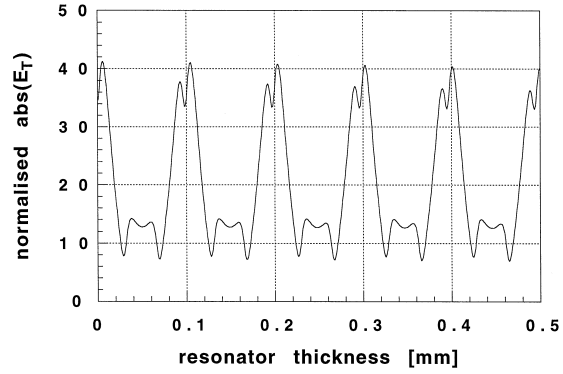

Fig. 10. Field enhancement due to the Fabry–Perot effect inside a Si slab at the third harmonic frequency.

Nevertheless, the effect of a standing wave inside the sample is very pronounced and can obviously be enhanced quite considerably by an increased reflectivity of the sample surfaces. However, it is not obvious how to achieve this experimentally. Metallic meshes applied to the sample surfaces could be a solution, however, preliminary experiments in this direction have not been successful [24], probably because the far-field approximation usually applied to the treatment of these meshes breaks down at the small distances imposed by the thin samples considered. There is nevertheless hope that the problem imposed by the small power conversion efficiency achieved in experiments so far may find a solution in this direction.

8. Conclusions

A THz radiation source in the power range of 10–100 kW will be required for collective Thomson scattering in fusion-oriented plasma devices. Such sources do not currently exist and with the only conceivable source, the free-electron laser, neither the required pulse length nor the narrow spectral width can be achieved. With gyrotrons, on the other hand, these parameters can be reached, but gyrotrons do not operate at THz frequencies. In this paper two methods have been discussed to convert gyrotron

radiation to the required high frequencies. With neither of these methods the desired results have been achieved yet, but current experiments seek to provide a proof of principle and to allow extrapolation.

Both cylindrical and quasi-optical gyrotrons have been operated at harmonic frequencies. It is difficult to achieve operation at one frequency only: in general some emission at the fundamental frequency is observed as well. Quasi-optical gyrotrons with Fabry–Perot type resonators incorporating a diffraction grating as output coupler are able to suppress undesired lower harmonics very efficiently. Experiments with such a device have been reported [11], but so far only at the fundamental frequency. A feasibility demonstration experiment for the third harmonic is in preparation at CRPP and first results can be expected towards the end of 1998.

Passive harmonic generation of gyrotron radiation in semiconductor materials has been reported several years ago. The major problem encountered is the low efficiency of this process. We have discussed several possibilities to improve the situation, in particular (1) careful choice of materials, (2) cooling to liquid nitrogen temperature and (3) the use of multi-pass structures. There is considerable hope to achieve the desired threshold value of 10% conversion efficiency, but this has not been demonstrated yet.

While harmonics higher than the third can in principle also be considered in both situations, the power obtained is even lower. They do offer the advantage that the fundamental frequency falls into a range where high power operation of gyrotrons has been demonstrated. If 1 to 1.5 THz is the aim, third harmonic operation means that the fundamental frequency is in the 300 to 500 GHz range. Such gyrotrons do exist, but are not able to produce the required power. A two-stage process could thus be considered: passive frequency conversion of a third harmonic gyrotron. However, this would only make sense if both stages could operate with high enough efficiency.

Acknowledgements

This work was partly supported by the Swiss National Science Foundation. The authors would like to thank P. Nikkola for his contribution to the design study of the 280 GHz quasi-optical gyrotron operating at the third harmonic.

References

[1] EU Home Team Report on ITER Diagnostics Task 1996/97.
[2] K. Sakamoto, A. Kasugai, M. Tsuneoka, K. Takahashi, Y. Ikeda, T. Imai, T. Kariya, Y. Mitsunaka, in: J. Parker, R.P. Smith (Ed.), Conf. Digest, 23rd Int. Conference on Infrared and Millimeter Waves, Colchester, U.K., 7–11 Sept. 1998, p. 363.
[3] G. Link, L. Feher, S. Rhee, M. Thumm, in: J. Parker, R.P. Smith (Ed.), 23rd Int. Conference on Infrared and Millimeter Waves, Colchester, U.K., 7–11 Sept. 1998, p. 377.
[4] K.E. Kreischer, C. Farrar, R.G. Griffin, R.J. Temkin, in: J. Parker, R.P. Smith (Ed.), 23rd Int. Conference on Infrared and Millimeter Waves, Colchester, U.K., 7–11 Sept. 1998, p. 357.
[5] V.E. Myasnikov, S.V. Usachev, M.V. Agapowa, V.V. Alikaev, G.G. Denisov, A.Sh. Fix, V.A. Flyagin, A.Ph. Gnedenkov, V.I. Ilyin, A.N. Kuftin, L.G. Popov, V.E. Zapevalov, in: J. Parker, R.P. Smith (Ed.), 23rd Int. Conference on Infrared and Millimeter Waves, Colchester, U.K., 7–11 Sept. 1998, p. 24.
[6] K. Felch, P. Borchard, S. Cauffman, R.W. Callis, P. Cahalan, T.S. Chu, D. Denison, H. Jory, M. Mizuhara, D. Remsen, G. Saraph, R.J. Temkin, in: J. Parker, R.P. Smith (Ed.), 23rd Int. Conference on Infrared and Millimeter Waves, Colchester, U.K., 7–11 Sept. 1998, p. 367.
[7] T. Idehara, I. Ogawa, S. Mitsudo, M. Pereyaslavets, in: J. Parker, R.P. Smith (Ed.), 23rd Int. Conference on Infrared and Millimeter Waves, Colchester, U.K., 7–11 Sept. 1998, p. 314.
[8] S. Alberti, M. Pedrozzi, M.Q. Tran, J.P. Hogge, T.M. Tran, P. Muggli, B. Jödicke, H.G. Mathews, Phys. Fluids B 11 (1990) 2544–2546.
[9] T.M. Tran, G. Jost, K. Appert, S. Alberti, M. Pedrozzi, Phys. Plasmas 4 (8) (1997) 3043–3048.
[10] M.Q. Tran, H. Cao, J.-P. Hogge, W. Kasparek, T.M. Tran, P.J. Paris, J. Appl. Phys. 73 (5) (1993) 2089–2102.
[11] J.-P. Hogge, T.M. Tran, P.J. Paris, M.Q. Tran, Phys. Plasmas 3 (9) (1996) 3492–3500.
[12] R. Gruber, S. Merazzi, T.M. Tran, DAPHNE: A programming environment for gyrotron optimization, in: M.Q. Tran (Ed.), Proc. 16th Int. Conference on Infrared and Millimeter Waves, Lausanne, SPIE Vol. 1240, 1991, pp. 535–536.
[13] F. Dufaux, Etude Théorique de l'émission harmonique dans un gyrotron quasi-optique, Diplôme du Département de Physique de l'Ecole Polytechnique Fédérale de Lausanne, 1990.
[14] M. Pedrozzi, S. Alberti, J.-P. Hogge, M.Q. Tran, T.M. Tran, Phys. Plasmas 5 (6) (1998) 2421–2430.
[15] V.L. Bratman, O. Dumbrajs, P. Nikkola, A.V. Savilov, On the negative mass instability as a source of electron energy

spread in gyrotrons, Proc. ITG-Conference, Display and Vacuum Electronics, Garmisch-Partenkirchen, Germany, 1998.
[16] S. Schiller, J. Mlynek, Phys. Bl. 50 (1994) 459–461.
[17] F. Keilmann, Proc. SPIE 666 (1986) 193.
[18] A. Mayer, F. Keilmann, Phys. Rev. B 33 (1989) 6962.
[19] F. Keilmann, R. Brazis, H. Barkley, W. Kasparek, M. Thumm, V. Erckmann, Europhys. Letters 11 (4) (1990) 337.
[20] M.R. Siegrist, F. Keilmann, Ch. Nieswand, M. Urban, Infrared Physics and Technology 36 (1995) 407.
[21] M. Urban, Ch. Nieswand, M.R. Siegrist, F. Keilmann, J. Appl. Phys. 77 (1995) 981.
[22] M. Urban, M.R. Siegrist, L. Asadauskas, R. Raguotis, R. Brazis, Lithuanian J. Phys. 35 (1995) 430.
[23] M. Urban, M.R. Siegrist, L. Asadauskas, R. Raguotis, R. Brazis, Appl. Phys. Lett. 69 (1996) 1776.
[24] M. Urban, Third harmonic generation of high power far infrared radiation in semiconductors, PhD Thesis No. 1492, EPFL, Lausanne, 1996, p. 105.
[25] R.W. Terhune, P.D. Maker, C.M. Savage, Phys. Rev. Lett. 8 (1962) 404.
[26] P.A. Lebwohl, J. Appl. Phys. 44 (1979) 1744.
[27] R. Brazis, R. Raguotis, M.R. Siegrist, Suitability of drift nonlinearity in Si, GaAs and InP for high power frequency converters with a 1 THz radiation output, accepted for publication in J. Appl. Phys.